Geodetic Slip Model of the 3 September 2016 M_w 5.8 Pawnee, Oklahoma, Earthquake: Evidence for Fault-Zone Collapse

by Fred F. Pollitz, Charles Wicks, Martin Schoenball, William Ellsworth, and Mark Murray

ABSTRACT

The 3 September 2016 M_w 5.8 Pawnee earthquake in northern Oklahoma is the largest earthquake ever recorded in Oklahoma. The coseismic deformation was measured with both Interferometric Synthetic Aperture Radar and Global Positioning System (GPS), with measureable signals of order 1 cm and 1 mm, respectively. We derive a coseismic slip model from Sentinel-1A and Radarsat 2 interferograms and GPS static offsets, dominated by distributed left-lateral strike slip on a primary west-northwest–east-southeast-trending subvertical plane, whereas strike slip is concentrated near the hypocenter (5.6 km depth), with maximum slip of ~1 m located slightly east and down-dip of the hypocenter. Based on systematic misfits of observed interferogram line-of-sight (LoS) displacements, with LoS based on shear-dislocation models, a few decimeters of fault-zone collapse are inferred in the hypocentral region where coseismic slip was the largest. This may represent the postseismic migration of large volumes of fluid away from the high-slip areas, made possible by the creation of a temporary high-permeability damage zone around the fault.

Electronic Supplement: Table of relocated seismicity, ascending orbit interferograms, and figures of slip inversion results.

INTRODUCTION

Moderate-magnitude seismicity has greatly accelerated in the central United States since about 2009, coincident with the commencement of large-scale injection of wastewater into the shallow crust (Ellsworth, 2013; Ellsworth *et al.*, 2015; McGarr *et al.*, 2015). The 3 September 2016 M_w 5.8 earthquake was the second $M \geq 5$ earthquake to strike Oklahoma in 2016 (Fig. 1a) and the largest earthquake ever recorded in Oklahoma. Practically, all regional seismicity occurs at shallow depth $\lesssim 5$ km, that is, near the top of the crystalline basement (Ellsworth, 2013; Walsh and Zoback, 2015), but coseismic slip and aftershocks may penetrate up to ~10 km in larger events, such as the 2011 M_w 5.6 Prague, Oklahoma, earthquake (Keranen *et al.*, 2013; Sun and Hartzell, 2014).

The Pawnee earthquake is the first in Oklahoma to be associated with measurable coseismic deformation, which is on the order of 1 cm at the Earth's surface. The distribution of aftershocks and the focal mechanism (Fig. 1b) suggest that the earthquake involved left-lateral strike slip on a previously unknown west-northwest–east-southeast-trending fault that intersects the mapped northeast–southwest-trending Labette fault zone. Here we assemble data from Interferometric Synthetic Aperture Radar (InSAR) and Global Positioning System (GPS) to investigate the distribution of coseismic slip associated with the earthquake. We shall consider distributed slip models that involve shear dislocations on the causative fault plane(s) as well as fault-zone collapse, a postseismic process that has been previously invoked to explain crustal deformation observed after the 1989 M_w 6.9 Loma Prieta, California, earthquake (Savage *et al.*, 1994; Bürgmann *et al.*, 1997), 1992 M_w 7.3 Landers, California, earthquake (Massonnet *et al.*, 1996; Savage and Svarc, 1997), 1999 M_w 7.1 Hector Mine, California, earthquake (Jacobs *et al.*, 2002), and 2003 M_w 6.6 Bam, Iran, earthquake (Fielding *et al.*, 2009). We find that fault-zone collapse appears necessary to replicate the geodetic data, particularly strong asymmetry in the InSAR-measured ground deformation observed in adjacent quadrants that is inconsistent with models of pure strike slip.

DATASET

We assembled Synthetic Aperture Radar (SAR) pairs from the C-band (5.54 cm wavelength) Sentinel-1A satellite of the European Space Agency and Radarsat 2 satellite of the Canadian Space Agency that spanned the time of the Pawnee earthquake with short perpendicular baselines. Interferograms were processed with the GAMMA software suite. Precise orbits were used to process the Sentinel scenes (see Data and Resources). Topographic phase was removed from interferograms using the

doi: 10.1785/0220170002

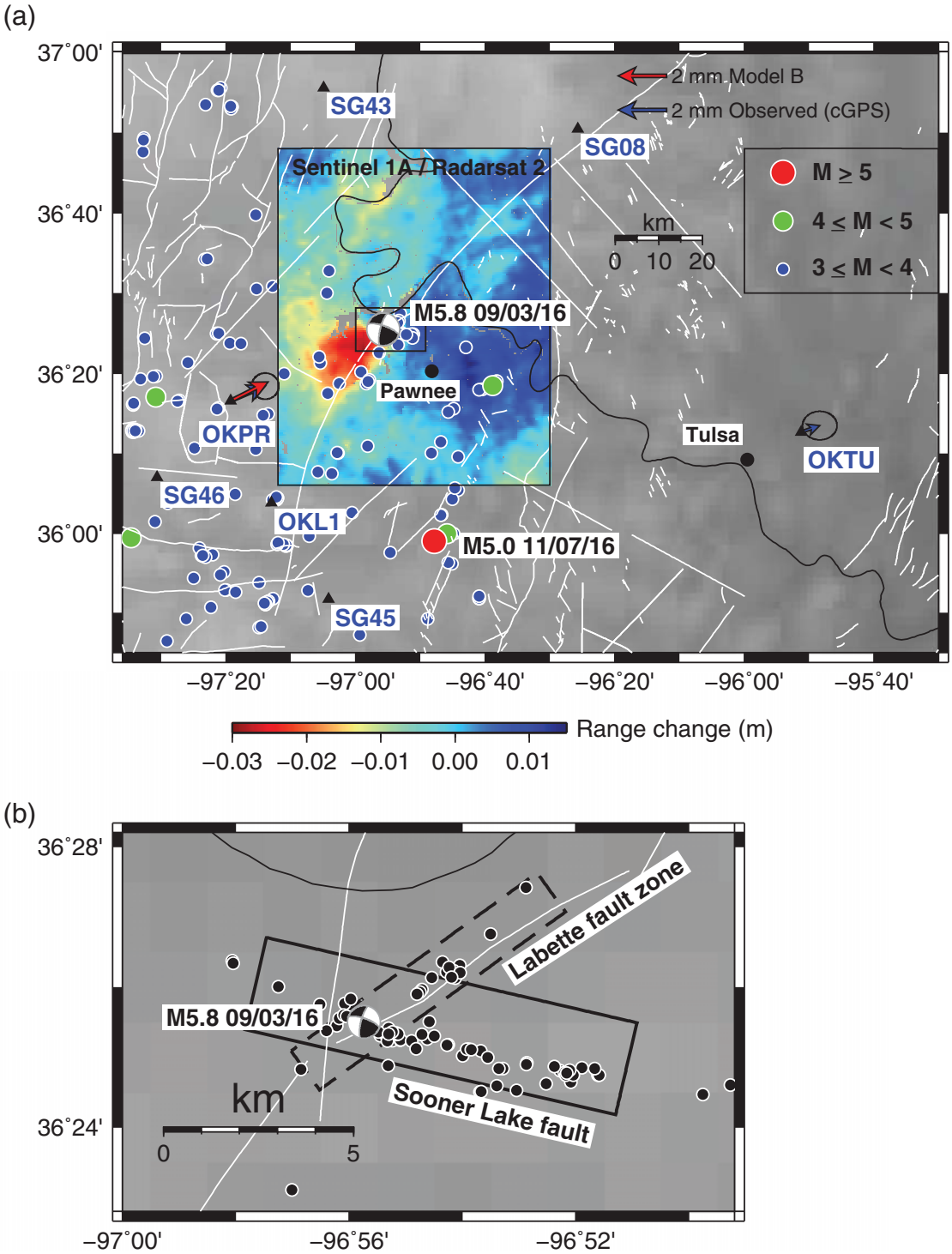

▲ **Figure 1.** (a) Magnitude ≥ 3 seismicity of northern Oklahoma from 1 January 2016 to 22 November 2016 from the National Earthquake Information Center (NEIC) catalog. Superimposed is the focal mechanism of the 3 September 2016 M_w 5.8 Pawnee earthquake. Horizontal coseismic displacements (black vectors with 95% errors) are shown for two sites within 100 km of the epicenter, together with the locations of other nearby Global Positioning System (GPS) sites. The stacked interferogram is that of Figure 2c. Model horizontal displacements based on the model B slip distribution (Table 2 and Fig. 8) are shown with red vectors. White lines indicate interpretative Oklahoma faults. (b) Relocated M ≥2.0 aftershocks occurring within the first 14 days of the 3 September 2016 mainshock. The solid rectangle indicates the outline of the primary plane, and the dashed rectangle the secondary plane, upon which distributed slip is imposed. The primary plane passes through the mainshock hypocenter and has upper and lower edge depths of 2 and 12 km, respectively, and the secondary plane passes through the mainshock hypocenter and has upper and lower edge depths of 2 and 8 km, respectively. The new fault represented by the primary plane is named the Sooner Lake fault by Oklahoma Geological Survey.

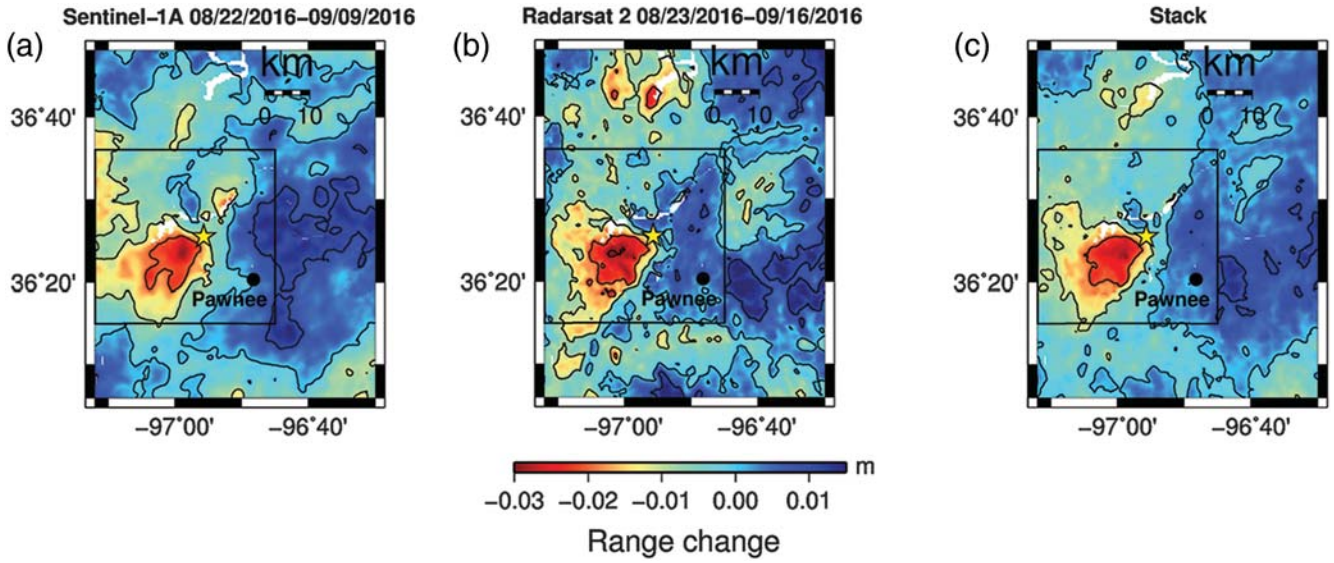

▲ **Figure 2.** Observed interferograms spanning the 3 September 2016 Pawnee, Oklahoma, earthquake from (a) Sentinel-1A spanning 22 August 2016 to 9 September 2016, (b) Radarsat 2 spanning 23 August 2016 to 16 September 2016, and (c) the stack consisting of the average of the line-of-sight (LoS) displacements in (a) and (b). LoS displacement from the boxed area is used to constrain the slip models. In all subplots, the small yellow star denotes the NEIC epicenter.

1 arcsec void-filled Shuttle Radar Topography Mission (SRTM) plus digital elevation model (DEM; Farr *et al.*, 2007; see Data and Resources). Interferograms were processed using multilooks that yielded ground pixels that closely matched the resolution of the DEM (for Radarsat 2, 3 in range and 6 in azimuth; for Sentinel, 8 in range and 2 in azimuth). The interferograms were filtered using an adaptive filter (based on Goldstein and Werner, 1998), with an alpha value of 0.6. The interferograms were masked with values of coherence above 0.9 and then unwrapped with a minimum cost flow procedure (Constantini, 1998).

We selected two such pairs, Sentinel-1A spanning 22 August 2016 to 9 September 2016 and Radarsat 2 spanning 23 August 2016 to 16 September 2016, and formed interferograms that exhibit clear visual signals associated with the earthquake (Fig. 2). Both are ascending-orbit inteferograms with similar heading and eastward radar incidence angles (Sentinel-1A heading and incidence angle 350.1° and 41.3°; Radarsat 2 heading and incidence angle 349.8° and 39.8°), and hence positive line-of-sight (LoS) displacements represent upward or westward motion. The interferograms exhibit a quadrant pattern roughly consistent with left-lateral strike slip on a west-northwest–east-southeast-trending subvertical fault, as indicated by the focal mechanism. However, the positive northwest and negative southwest lobes of LoS displacement are strongly asymmetric in both interferograms, with the southwest lobe having LoS displacement of ~ -2.5 cm and the northwest-quadrant LoS displacement of $\sim +0.5$ cm. This is in accord with an independent analysis of Sentinel-1A SAR by Yeck *et al.* (2016), using the same preseismic acquisition on 22 August 2016. We have additionally processed Sentinel-1A and Radarsat 2 interferograms spanning the mainshock over other periods (see Ⓔ Fig. S1, available in the electronic supplement to this article), and their composite also shows strong asymmetry between the southwest and northwest quadrants. This asymmetry is not compatible with models of coseismic strike slip alone.

The earthquake-generated signal is disrupted by nontectonic signals of similar amplitude likely arising from water vapor variations in the troposphere. Hence the signal-to-noise ratio is roughly 1:1 within ~20 km of the rupture but diminishes rapidly at greater distance. The signal is likely stronger in the stacked interferogram (Fig. 2c), which is the average of the Sentinel-1A interferogram (Fig. 2a) and the Radarsat 2 interferogram (Fig. 2b).

GPS data have been collected by the State of Oklahoma Department of Transportation as part of the Continuously Operating Reference Station (CORS) Associated Networks ("OK" sites in Fig. 1a; see Data and Resources) and by SuomiNet-G administered by UNAVCO (Ware *et al.*, 2000). Continuous GPS time series are available at two sites within 100 km of the earthquake epicenter and permit a determination of static offsets (Fig. 3). We use the GPS time series processed by the University of Nevada, Reno, to 24-hr solutions in the NA12 reference frame (Blewitt *et al.*, 2013) beginning 1.5 yrs prior to the earthquake up to 2.5 months after the earthquake. For a given horizontal component, the time series is fit with a line of constant slope appended by seasonal (annual and semiannual) terms as well as the coseismic displacement jump at the time of the earthquake. The closest GPS site, OKPR, about 35 km southwest of the epicenter, moved about 1.6 ± 0.3 mm toward the northeast. The eastward offset of 0.8 mm estimated at OKTU is apparently significant, but the formal error of ~0.3 mm may be unrealistically low given the one-month data gap just prior to the earthquake. Data spanning

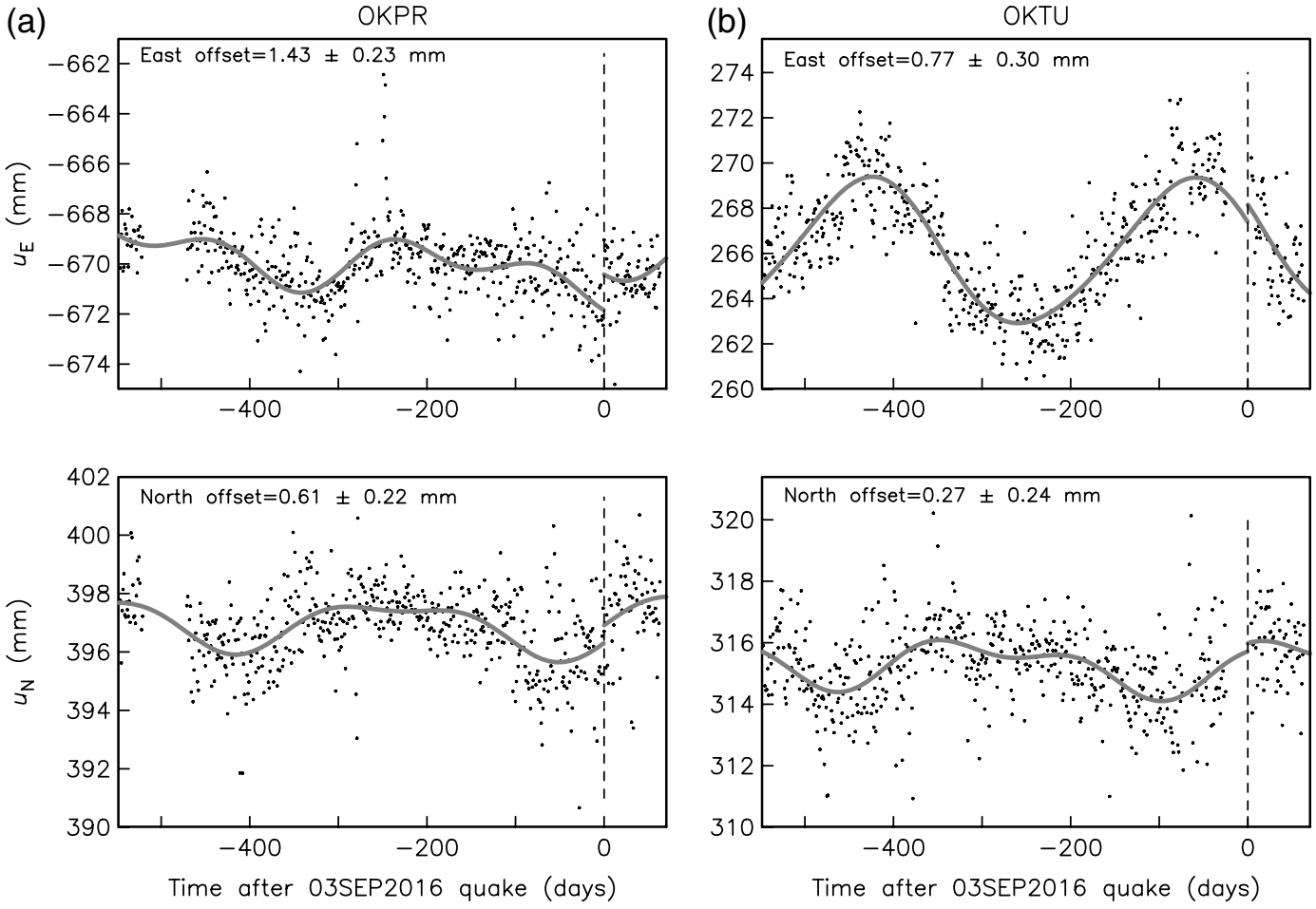

▲ **Figure 3.** GPS time series for (a) OKPR and (b) OKTU in the NA12 reference frame (Blewitt *et al.*, 2013). Each time series has been least-squares fit with a model that includes a linear function of time, seasonal terms, and a coseismic offset.

the time of the earthquake are unavailable for others sites (OKL1 and the SuomiNet-G sites), many of which were unable to collect data due to a receiver firmware problem handling the GPS week rollover in February 2016 (J. Normandeau, personal comm., 2016). Following the methods used by the UNAVCO Geodesy Advancing Geosciences and Earthscope (GAGE) Facility (Herring *et al.*, 2016), we repeated the estimation of coseismic offsets using GPS time series processed by UNAVCO, and the estimated coseismic offsets are very close to the preceding estimates for the horizontal components of both OKPR and OKTU.

EARTHQUAKE RELOCATIONS

We relocated 288 earthquakes cataloged by the Oklahoma Geological Survey (OGS) for the period 1 August 2016 through 22 November 2016 using regional and temporary stations available through Incorporated Research Institutions for Seismology. Only stations closer than 0.6° were used before the bulk of temporary deployments became online around 12 October 2016, and stations closer than 0.3° after that, respectively. Our velocity model (Table 1) is based on a study of regional seismicity using the code Velest (Kissling *et al.*, 1994). The basement depth is assigned to be 1.5 km below the surface, consistent with regional geology (Fig. 4). We use a constant V_P/V_S ratio of 1.78. Absolute locations were obtained using HYPOINVERSE-2000 (Klein, 1994). Formal location uncertainties in the horizontal are on the order of 0.4 km initially and decrease to around 0.2 km when the temporary stations come online. Vertical uncertainties are usually less than 1 km. To image the structure illuminated by the aftershocks, we derive high-precision relative locations using hypoDD (Waldhauser and Ellsworth, 2000). In the first iterations of hypoDD, we only use differential times derived from catalog pick times to constrain the overall structure of the aftershock zone. In later iterations and for event separations less than 2 km, we fold in differential travel times measured using cross-correlation time lags and decrease the weight of the less-precise catalog picks. Waveforms were band-pass filtered between 2 and 20 Hz. Subsample precision is achieved following the approach of Deichmann and Garcia-Fernandez (1992) by fitting a parabola through the five samples closest to the sample with the highest cross-correlation coefficient. We performed the cross correlations on all components, taking the one yielding the highest cross-correlation coefficient to measure the differential

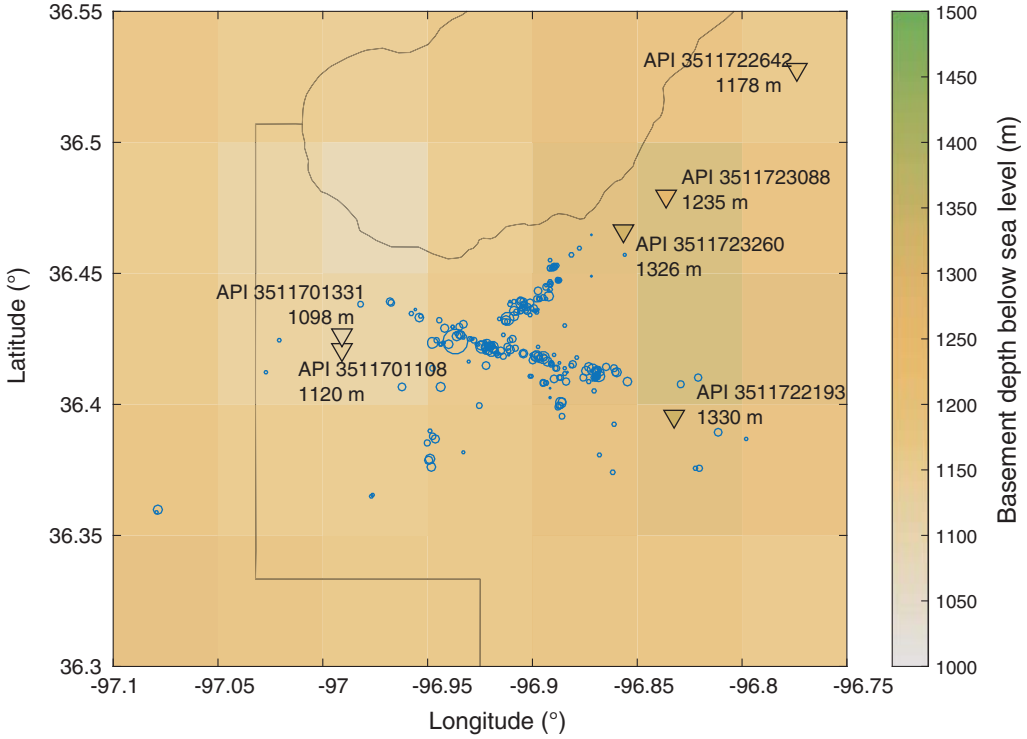

▲ **Figure 4.** Map of basement depth obtained from kriging of basement top data (Campbell and Weber, 2006) from wells in the area (triangles). Annotations refer to top of basement below sea level. Aftershocks are shown as blue circles scaled by magnitude.

travel time. We required a cross-correlation coefficient of at least 0.7 to retain this differential time measurement.

Most of the aftershocks are distributed along two dominant trends (Fig. 1b), but additional scattered seismicity is located throughout the region. The southern trend corresponds to one of the two nodal planes of the moment tensor solution. The northern trend included some activity before the mainshock. An M_w 2.3 event occurred on 10 August 2016, and two events with magnitudes 2.6 and 3.0 occurred four and two days prior to the mainshock, respectively. The mainshock is located at 3.6-km depth with an uncertainty of 0.7 km, near the intersection of the two aftershock trends. The catalog of relocated hypocenters is provided in Ⓔ Table S1.

To obtain the strikes and dips of the main active fault trends, we manually selected events of each principal fault trend and determined the covariance matrix of the hypocenters, using a robust estimator to discard outliers, that is, events close to the main trend but not in the fault plane (Rousseeuw, 1984). This method yielded strikes and dips of the two main trends of 283°/77° and 234°/78°, respectively (Fig. 5). These orientations are consistent with results of a RANSAC algorithm (Fischler and Bolles, 1981), with which we attempted to fit the largest number of events within a cuboid of a given threshold width but unconstrained length, height, and position.

Table 1
Regional Velocity Model

Top (km)	V_P (km/s)	V_S (km/s)
0.0	2.70	1.52
0.3	2.95	1.68
1.0	4.15	2.33
1.5	5.80	3.26
8.0	6.27	3.52
21.0	6.41	3.60

COSEISMIC SLIP MODEL

To explain the InSAR and GPS coseismic displacements, we constructed a dislocation model allowing distributed slip on two planes determined by analysis of aftershocks described in the Earthquake Relocations section. First, we allowed for left-lateral strike slip, reverse slip, and fault-zone collapse on a primary plane of dimensions 10 km (along strike) × 10.51 km (along dip) passing through the National Earthquake Information Center (NEIC) hypocenter (36.425° N, 96.929° W, depth 5.6 km) and with strike equal to 283° and dip equal to 77°. We chose this west-northwest–east-southeast-trending plane as the primary plane because the great majority of aftershocks were located along this trend (Fig. 1b), and the focal mechanisms of several aftershocks are consistent with left-lateral strike slip on this plane (Yeck *et al.*, 2016). The new fault represented by this plane is named the Sooner Lake fault by OGS (Fig. 1b). The along-dip dimension allows for slip on the 77°-dipping plane between upper and lower edge depths of 2 and 12 km, respectively. Second, we allow for right-

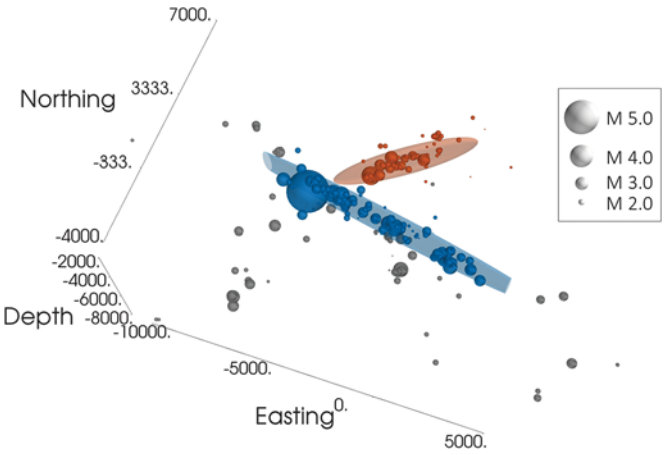

▲ **Figure 5.** 3D view of relocated seismicity. Blue and red events are selected for fitting the mainshock (primary) plane and aftershock (secondary) plane, respectively, determined through an adaptive RANSAC algorithm (Fischler and Bolles, 1981). The ellipsoid represents the orientation of the eigenvectors of the robust covariance matrix.

lateral slip on an 8-km-long secondary plane with strike 234° N and dip 78°, also constrained to pass through the NEIC hypocenter and with upper and lower edge depths of 2 and 8 km, respectively (Fig. 1b). We choose the NEIC hypocentral depth of 5.6 km in further analysis, which is slightly deeper than the depth determined from the HYPOINVERSE-2000 analysis in the Earthquake Relocations section.

Each fault plane is discretized into 108 separate patches, and displacement Green's functions for uniform slip on each patch are calculated using the STATIC1D code (Pollitz, 1996) applied to a layered elastic model. This is a three-layer model with a sedimentary layer in the upper 1.5 km (shear modulus $\mu = 18$ GPa), basement rock from 1.5 to 42 km depth ($\mu = 35$ GPa), and underlying mantle ($\mu = 68$ GPa). The 1.5 km depth to the top of the basement is based on well data (Fig. 4). The deeper elastic structure is consistent with the regional seismic structure (e.g., Elebiju *et al.*, 2011; Laske *et al.*, 2013). The Green's functions for LoS displacement assume an ascending orbit with azimuth 350.1° and a radar incidence angle of 41.2° (looking toward the east).

Slip distributions are designed to minimize an objective function consisting of the summed squared misfit to horizontal GPS and LoS displacements. We use simulated annealing with a weak amount of smoothing to derive the slip distributions subject to positivity constraints on slip. Specifically, strike slip must be left-lateral on the primary plane and right-lateral on the secondary plane, and dip slip must be reverse slip on the primary plane, based on the rake of 13° obtained in the NEIC solution; dip slip is assumed negligible on the secondary plane. Fault-zone collapse, when included in the slip model, is also constrained to be positive on the primary plane. InSAR data were subsampled within a smaller region more closely centered on the epicenter (boxed area of each interferogram in Fig. 2). We performed slip inversions with the stacked interferogram of Figure 2c, appended by the horizontal GPS offsets for the two sites of Figure 1a. Three additional parameters (a uniform shift and tilt in the north and east directions) are introduced to model LoS displacement. The GPS offsets were assigned a relatively small weight that has little effect on the inversion results, because even with little weight we find that all models fit the OKPR offsets well.

The smoothing is implemented as additional terms in the objective function proportional to the squared slip gradient integrated over each fault plane and summed over each slip component. The weights of these terms are identical in all inversions. The weights were chosen to yield maximum slip not exceeding 1–2 m. Slip models yielding practically the same level of fit may be obtained without smoothing but exhibit large, localized slip of several meters. The sensitivity of slip inversion results to the assumed weights is shown in Ⓔ Figures S2–S4, which provide a picture of the range of possible slip distributions. A more complete slip inversion procedure, that is, Markov Chain Monte Carlo (MCMC) (Fukuda and Johnson, 2008) would permit a better picture of the model errors.

In a first set of slip models, we allowed for distributed strike slip and dip slip on the primary plane (model A of Table 2). The estimated dip slip is found to be negligible, less than 1% of the average amount of strike slip, and so we restrict attention to the estimation of distributed left-lateral strike slip. For one-plane-distributed slip models restricted to the primary plane, the obtained strike slip is shown in Figure 6. Model A predicted LoS displacements are shown in Figure 7a and the corresponding residual interferogram in Figure 7d. This model captures the chief features of the observed interferograms, including the positive and negative LoS lobes northwest and southwest of the epicenter, respectively, and the broad region of positive LoS to the east.

A second type of slip model involves a combination of left-lateral strike slip and fault-zone collapse on the primary fault

Table 2
Summary of Model Faults and Results

Model Class	Primary Plane Slip	Secondary Plane Slip	InSAR Model Figures	Slip Model Figures
A	Left-lateral strike slip + reverse slip	–	7a,d	6
B	Left-lateral strike slip + fault-zone collapse	–	7b,e	8
C	Left-lateral strike slip + fault-zone collapse	Right-lateral strike slip	7c,f	9

InSAR, Interferometric Synthetic Aperture Radar.

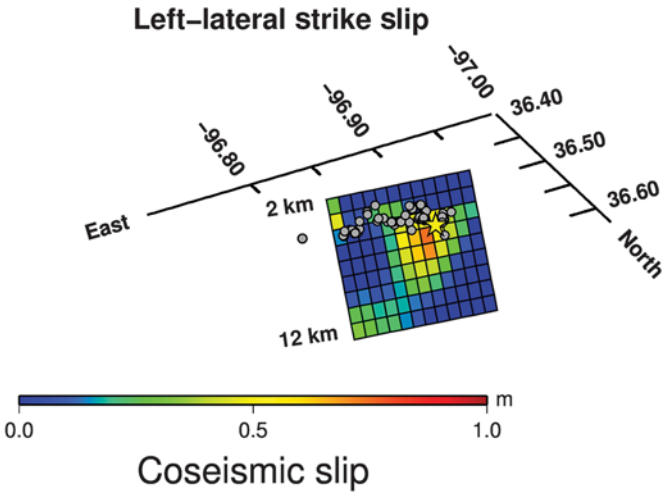

▲ **Figure 6.** Distribution of coseismic left-lateral strike slip obtained in model A (Table 2) from inverting the stacked interferogram (Fig. 2c), appended with GPS horizontal displacements. The view is from the northeast. Superimposed are the NEIC hypocenter (yellow star) and hypocenters of aftershocks during the first 14 days after the mainshock that are within 0.5 km of the primary plane (gray circles).

plane (model B of Table 2). Because the ~1-month-long time periods spanned by the interferograms extend one to two weeks after the earthquake, fault-zone collapse may contribute to observed InSAR LoS as an early postseismic process. In modeling this case, the fault-zone collapse component is constrained to not exceed one-half the strike-slip component, and the slip optimization uses the same regularization on slip as imposed previously. The resulting slip distribution in Figure 8 has up to one meter of left-lateral strike slip and a few decimeters of fault-zone collapse in the region around the hypocenter associated with high coseismic strike slip. The moment magnitude of the left-lateral strike-slip component is 5.79. Because this moment estimate is based on geodetic data collected over a time window that extends well past the time of rupture, the inferred moment magnitude may be overestimated, due to the inclusion of postseismic creep.

DISCUSSION

The slip distribution of Figure 6 has slip concentrated just east and down-dip of the hypocenter. It indicates coseismic slip of up to 1 m and extending down to ~9 km. Seismicity is concentrated on the periphery of the high-coseismic-slip region, similar to the finding of Johanson *et al.* (2006) for the 2004 Parkfield, California, earthquake. We find that the fit of the stacked interferogram is better than the fit achieved with fitting either of the individual interferograms, suggesting that stacking is reinforcing the coseismic deformation signal and partially diminishing atmospheric noise.

In model B, the joint strike-slip and fault-zone collapse model (Fig. 8), the fault-zone collapse acts to reduce systematic misfit between observed and model LoS, that is, by reducing predicted LoS over the region west of the mainshock hypocenter, both in the northwest quadrant where model positive LoS greatly exceeds observed LoS and in the southwest quadrant where model negative LoS falls short of observed LoS in a model involving only shear dislocations (Fig. 7a). The improvement in both quadrants is clear in the model interferogram (Fig. 7b) and in the residual interferogram (Fig. 7e). Model horizontal displacements from this inversion are shown in Figure 1 and match the observed northeastward displacement at OKPR.

The inferred fault-zone collapse is likely a postseismic process that could represent compaction of cracks that developed during the coseismic rupture due to migration of fluids away from the fault zone. These processes were originally proposed to explain fault-normal contraction observed following the 1992 Landers, California, earthquake (Massonnet *et al.*, 1996; Savage and Svarc, 1997). Fluids are widely believed to be involved in the triggering of the majority of recent earthquakes in Oklahoma, as well as many earlier midcontinent earthquakes (e.g., McGarr *et al.*, 2002; Walsh and Zoback, 2015). An active mature fault may be surrounded by a relatively high-permeability core (e.g., Zoback *et al.*, 2011), providing fluid conduits to the fault. However, northcentral Oklahoma faults have generally little recent activity, and relatively inactive faults tend to exhibit low permeability around the fault (e.g., Sutherland *et al.*, 2012). Shah and Keller (2017) note that Oklahoma earthquakes tend to occur where the crystalline basement is composed of igneous intrusive or metamorphic rocks with well-developed fracture networks, and these provide fluid pathways to and from the fault. Once fluids migrate from deeper sedimentary formations to the underlying crystalline basement, the increased fluid pressure reduces the normal stress on the fault and triggers earthquakes (e.g., National Research Council, 2012). During an earthquake, a very high-permeability damage zone may develop around the fault for a short time before collapse of fluid pathways restores permeability to roughly its prequake state (Li *et al.*, 2003). The compaction process may involve the expulsion of large volumes of fluids if they were initially present. Regardless of the mechanism, our inferred fault-zone collapse is evidently considerably deeper than 1– ~ 4 km depth documented for some naturally occurring earthquakes, for example, the 1999 Hector Mine, California, earthquake (Jacobs *et al.*, 2002), or the 2003 Bam, Iran, earthquake (Fielding *et al.*, 2009). Deeper fault-zone collapse has been proposed for the 1989 Loma Prieta, California, earthquake, for which Savage *et al.* (1994) and Bürgmann *et al.* (1997) favor 0.1–0.2 m fault-normal closure at 5–16 km and 8–16.8 km depth, respectively, and for the 1992 Landers, California, earthquake, where Massonnet *et al.* (1996) infer fault closure of ~0.3 m between 6 and 11 km depth.

Some afterslip may have occurred on a northeast–southwest-trending plane roughly coincident with the southern end of the Labette fault zone and where a linear trend of early aftershocks occurred (Fig. 1b). The InSAR LoS may include afterslip for one to two weeks following the mainshock. This is

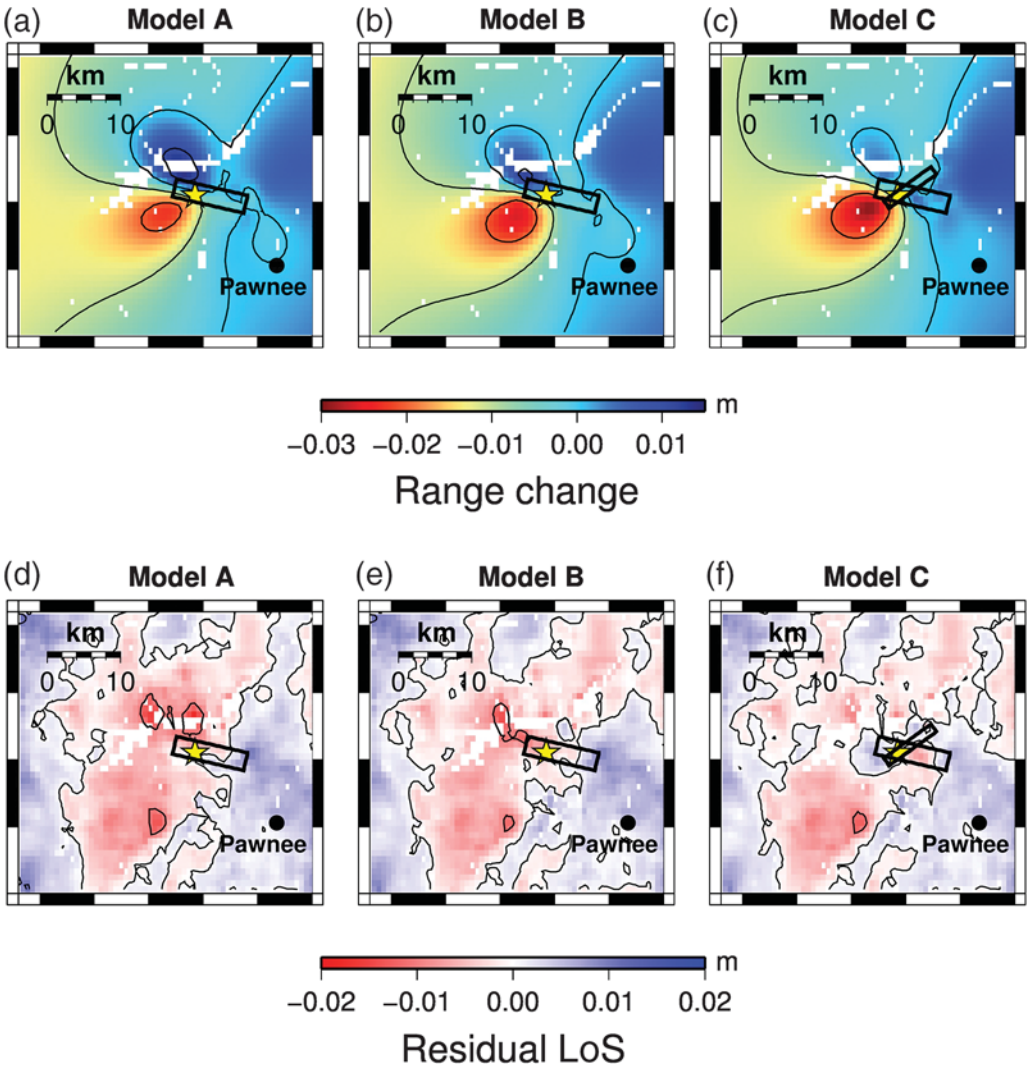

▲ **Figure 7.** Model interferograms from fitting the stacked interferogram of Figure 2c and observed horizontal GPS offsets (Fig. 1) with (a) one-plane (primary plane) model with shear dislocations (combined strike slip and dip slip), (b) a one-plane model with combined strike slip and fault-zone collapse, and (c) a two-plane (primary plane plus secondary plane) model. These are models A, B, and C, respectively, as described in Table 2. Corresponding residual LoS displacements (observed minus model) are shown in (d), (e), and (f). In all subplots, the small yellow star denotes the NEIC epicenter, and the surrounding rectangle is the surface projection of the fault plane(s) used in the dislocation modeling.

particularly relevant for the secondary plane, which emerges in the seismicity only gradually through aftershocks occurring within two weeks after the mainshock, later than the primary plane which hosts vigorous aftershock activity already during the first day after the mainshock. To test this, we derive distributed slip on both the primary and secondary planes. We permit both left-lateral strike slip and fault-zone collapse on the primary plane as before, augmented by right-lateral strike slip on the secondary plane (model C of Table 2). The inferred slip (Fig. 9) involves a concentration of (presumed) afterslip on the secondary plane just east and west of the hypocenter, coincident with the locations of aftershocks and slip on the primary plane similar to that inferred in the joint strike-slip and fault-zone collapse model (Fig. 8). The right-lateral slip on the secondary plane serves to further reduce predicted LoS in the northwest quadrant (Fig. 7c), resulting in reduced residuals in that quadrant (Fig. 7f) and further reducing the systematic misfit between observed and predicted LoS in the one-plane model involving only shear dislocations (Fig. 7a). Hence it is even more effective in this regard than the model of fault-zone collapse (Fig. 7b,e). The moment magnitude of the left-lateral strike-slip component on the primary plane is 5.77.

A more extensive InSAR analysis by Grandin *et al.* (2017) employs six preseismic and six postseismic SAR acquisitions, resulting in a composite coseismic interferogram that exhibits a southwest-quadrant peak LoS of ~ -2 cm and a northwest-quadrant peak LoS displacement of $\sim +1$ cm. Their coseismic slip model is based on a kinematic rupture model derived from

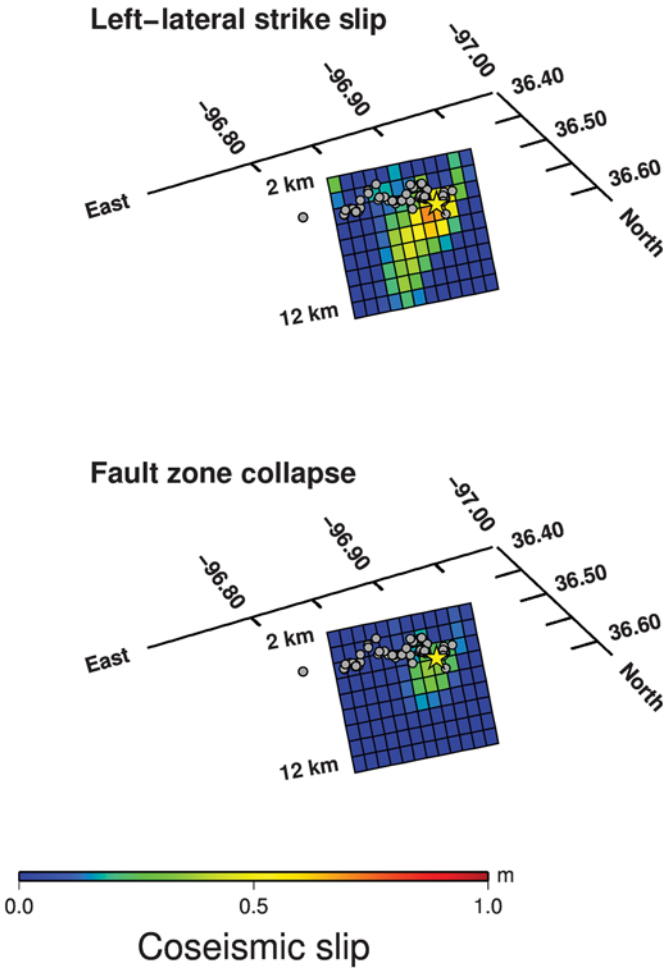

▲ **Figure 8.** Distribution of coseismic left-lateral strike slip and fault-zone collapse on the primary plane obtained in model B (Table 2) from inverting the stacked interferogram (Fig. 2c), appended with GPS horizontal displacements. The view is from the northeast. Superimposed are the NEIC hypocenter (yellow star) and hypocenters of aftershocks during the first 14 days after the mainshock (gray circles). These aftershocks have been edited into a group that lies within 0.5 km of the primary plane.

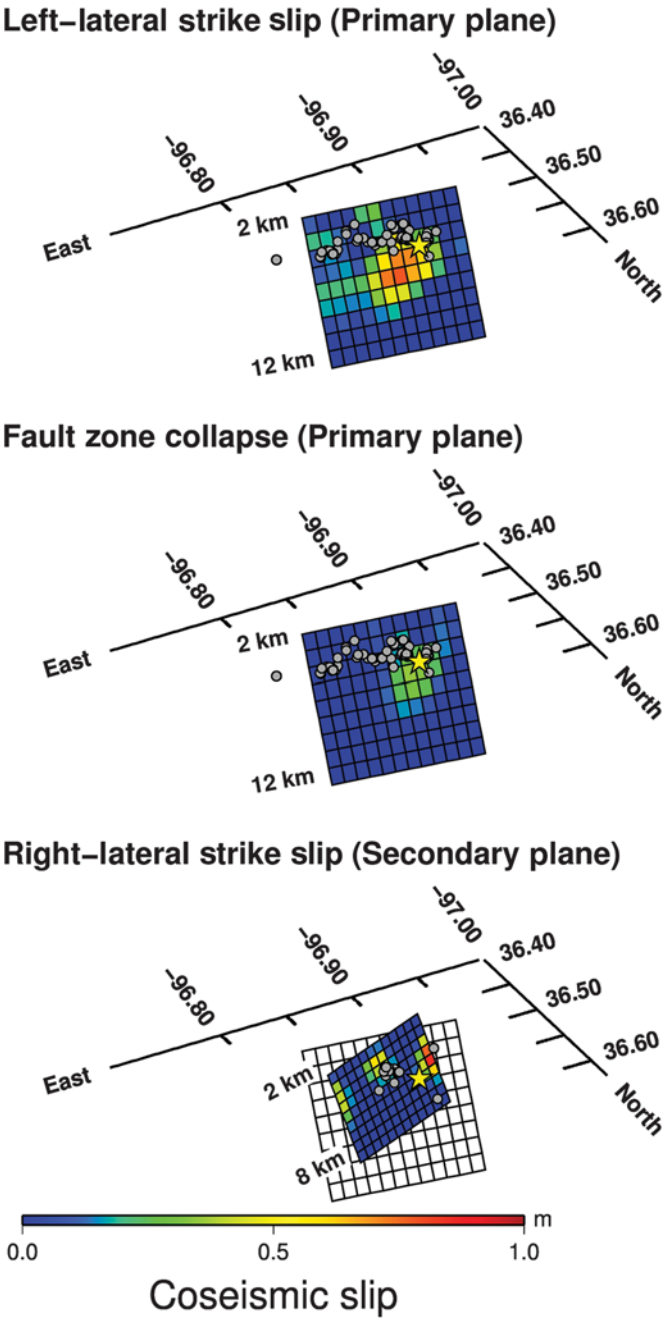

▲ **Figure 9.** Distribution of coseismic left-lateral strike slip and (likely postseismic) fault-zone collapse on the primary plane and (postseimic) right-lateral strike slip on the secondary plane obtained in model C (Table 2) from inverting the stacked interferogram (Fig. 2c), appended with GPS horizontal displacements. The view is from the northeast. Superimposed are the NEIC hypocenter (yellow star) and hypocenters of aftershocks during the first 14 days after the mainshock (gray circles). These aftershocks have been separated into groups that lie within 0.5 km of either plane.

joint geodetic and seismic-waveform data that invert for shear dislocations on the Sooner Lake fault. Predicted LoS displacement from the static limit of the kinematic slip model fits the composite interferogram well. Because the 2:1 ratio of southwest-quadrant displacement low to northwest-quadrant displacement high is less than the $>3:1$ ratio obtained here (Fig. 1c and Ⓔ Fig. S1c), little fault-zone collapse, if any, would be implied by their InSAR dataset. On the other hand, their model of left-lateral slip on the Sooner Lake fault shares the main features of our slip distribution; for example, the bulk of the slip is to the east and down-dip of the hypocenter.

A trade-off in slip between the primary and secondary planes is evident in differences between the primary-plane slip in the one-plane case (Fig. 6) and two-plane case (Fig. 9). In particular, the depth extent of inferred left-lateral slip on the primary plane diminishes substantially when both fault-zone collapse and afterslip are added to the model. Because of the limited resolution of our InSAR and GPS dataset, it may be difficult to separate left-lateral slip on the main

west-northwest–east-southeast-trending plane with any additional right-lateral slip on the secondary northeast–southwest-trending plane.

Coseismic slip extending well below the nucleation depth for the Pawnee event is similar to the coseismic slip pattern of the 2011 M_w 5.6 Prague, Oklahoma, event, which nucleated at shallow depth and ruptured down to ~10 km depth (Keranen *et al.*, 2013; Sun and Hartzell, 2014). It is consistent with the view that near-surface stress perturbations can trigger intraplate earthquakes that release tectonic strain that is stored in the continental lithosphere for long time periods (Craig *et al.*, 2016).

CONCLUSIONS

InSAR data spanning the time of the Pawnee earthquake combined with GPS horizontal coseismic displacements yield coseismic slip models of the earthquake. Assuming the west-northwest–east-southeast-trending plane of the NEIC focal mechanism and assuming shear dislocations only, this slip is almost entirely left-lateral strike slip. It has peak amplitude of ~1 m concentrated just east and down-dip of the hypocenter located in crystalline basement rock. Models involving only shear dislocations systematically mismatch the amplitude of LoS in both the northwestern and southwestern quadrants of observed interferograms. The observed LoS is much better explained by a combination of coseismic strike slip and postseismic fault-zone collapse of several decimeters in the areas of high coseismic strike slip. It may represent the expulsion of large volumes of fluid that had been present in the fault zone. We infer an additional few decimeters of postseismic right-lateral strike slip on a northeast–southwest-trending conjugate fault plane, coincident with the occurrence of aftershocks on a northeasterly trend from the mainshock hypocenter. Our geodetically derived slip distributions combined with the hypocentral depth of 5.6 km suggest that the Pawnee earthquake rupture initiated at relatively shallow depth and cascaded toward the east and down-dip to release accumulated tectonic strain.

DATA AND RESOURCES

Earthquake epicenters were provided by the National Earthquake Information Center (NEIC) and Oklahoma Geological Survey (OGS). Interferograms were provided by the European Space Agency (Sentinel-1A; https://earth.esa.int/web/guest/missions/esa-operational-eo-missions/sentinel-1, last accessed December 2016) and the Canadian Space Agency (Radarsat 2; www.asc-csa.gc.ca/eng/satellites/radarsat2/, last accessed December 2016). Global Positioning System (GPS) time series were provided by the University of Nevada, Reno (UNR) Geodesy Laboratory (http://geodesy.unr.edu, last accessed November 2016). Oklahoma faults were provided by the Oklahoma Fault Database (http://www.ou.edu/ogs/data/fault.html, last accessed December 2016). Some plots were made using the Generic Mapping Tools v.4.2.1 (www.soest.hawaii.edu/gmt, last accessed December 2016; Wessel and Smith, 1998). The other data are from the following websites: https://qc.sentinel1.eo.esa.int/aux_poeorb/, https://lpdaac.usgs.gov/about/news_archive/nasa_shuttle_radar_topography_mission_srtm_version_30_srtm_plus_product_release, and https://www.ngs.noaa.gov/CORS/organizations.shtml (all last accessed December 2016).

ACKNOWLEDGMENTS

We are grateful to Art McGarr and Jim Savage for internal reviews, and to Brett Carpenter, an anonymous reviewer, and to Editor-in-Chief Zhigang Peng for their constructive criticisms. We thank Earl Wilson and Brenda Ellis for help gaining access to the Radarsat 2 data. Schoenball and Ellsworth were supported by the Stanford Center for Induced and Triggered Seismicity, and Schoenball was partially supported by the Alexander von Humboldt Foundation.

REFERENCES

Blewitt, G., C. Kreemer, W. C. Hammond, and J. M. Goldfarb (2013). Terrestrial reference frame NA12 for crustal deformation studies in North America, *J. Geodyn.* **72,** 11–24.

Bürgmann, R., P. Segall, M. Lisowski, and J. L. Svarc (1997). Postseismic strain following the 1989 Loma Prieta earthquake from GPS and leveling measurements, *J. Geophys. Res.* **102,** 4933–4955.

Campbell, J. A., and J. L. Weber (2006). Wells drilled to basement in Oklahoma, *Oklahoma Geol. Surv. Spec. Publ., 2006–1*.

Constantini, J. L. (1998). A novel phase unwrapping method based on network programming, *IEEE Trans. Geosci. Remote Sens.* **36,** 813–821, doi: 10.1109/36.673674.

Craig, T. J., E. Calais, L. Fleitout, L. Bollinger, and O. Scotti (2016). Evidence for the release of long-term tectonic strain stored in continental interiors through intraplate earthquakes, *Geophys. Res. Lett.* **43,** 6826–6836, doi: 10.1002/2016GL069359.

Deichmann, N., and M. Garcia-Fernandez (1992). Rupture geometry from high-precision relative hypocentre locations of microearthquake clusters, *Geophys. J. Int.* **110,** 501–517, doi: 10.1111/j.1365-246X.1992.tb02088.x.

Elebiju, O. O., S. Matson, G. R. Keller, and K. J. Marfurt (2011). Integrated geophysical studies of the basement structures, the Mississippi Chert, and the Arbuckle Group of Osage County Region, Oklahoma, *AAPG J.* **95,** 371–394.

Ellsworth, W. L. (2013). Injection-induced earthquakes, *Science* **341,** no. 6142, doi: 10.1126/science.1225942.

Ellsworth, W. L., A. L. Llenos, A. F. McGarr, A. J. Michael, J. L. Rubenstein, C. S. Mueller, M. D. Petersen, and E. Calais (2015). Injection-induced earthquakes, *The Leading Edge* **34,** 618–626.

Farr, T. G., P. A. Rosen, E. Caro, R. Crippen, R. Duren, S. Hensley, M. Kobrick, M. Paller, E. Rodriguez, L. Roth, *et al.* (2007). The Shuttle Radar Topography Mission. *Rev. Geophys.* **45,** no. 2, doi: 10.1029/2005RG000183.

Fielding, E. J., P. R. Lundgren, R. Bürgmann, and G. J. Funning (2009). Shallow fault-zone dilatancy recovery after the 2003 Bam earthquake in Iran, *Nature* **458,** 64–68.

Fischler, M. A., and R. C. Bolles (1981). Random sample consensus: A paradigm for model fitting with applications to image analysis and automated cartography, *Commun. ACM* **24,** 381–395.

Fukuda, J., and K. Johnson (2008). A fully Bayesian inversion for spatial distribution of fault slip with objective smoothing, *Bull. Seismol. Soc. Am.* **98,** 1128–1146.

Goldstein, R. M., and C. L. Werner (1998). Radar interferogram filtering for geophysical applications, *Geophys. Res. Lett.* **25,** 4035–4038, doi: 10.1029/1998GL900033.

Grandin, R., M. Vallée, and R. Lacassin (2017). Rupture process of the Oklahoma M_w 5.7 Pawnee earthquake from Sentinel-1 InSAR and seismological data, *Seismol. Res. Lett.* **88,** no. 4, doi: 10.1785/0220160226.

Herring, T. A., T. I. Melbourne, M. H. Murray, M. A. Floyd, W. M. Szeliga, R. W. King, D. A. Phillips, C. M. Puskas, M. Santillan, and L. Wang (2016). Plate Boundary Observatory and related networks: GPS data analysis methods and geodetic products, *Rev. Geophys.* **54,** no. 4, doi: 10.1002/2016RG000529.

Jacobs, A., D. Sandwell, Y. Fialko, and L. Sichoix (2002). The 1999 (M_w 7.1) Hector Mine, California, earthquake: Near-field postseismic deformation from ERS interferometry, *Bull. Seismol. Soc. Am.* **92,** 1433–1442.

Johanson, I. A., E. J. Fielding, F. Rolandone, and R. Bürgmann (2006). Coseismic and postseismic slip of the 2004 Parkfield earthquake from space-geodetic data, *Bull. Seismol. Soc. Am.* **96,** S269–S282, doi: 10.1785/0120050818.

Keranen, K. M., H. M. Savage, G. A. Abers, and E. S. Cochran (2013). Potentially induced earthquakes in Oklahoma, USA: Links between wastewater injection and the 2011 M_w 5.7 earthquake sequence, *Geology* **41,** 699–702.

Kissling, E., W. L. Ellsworth, D. Eberhart-Phillips, and U. Kradolfer (1994). Initial reference models in local earthquake tomography, *J. Geophys. Res.* **99,** 19,635–19,646, doi: 10.1029/93JB03138.

Klein, F. W. (1994). Users guide to HYPOINVERSE-2000, a Fortran Program to solve for earthquake locations and magnitude, *U.S. Geol. Surv. Open-File Rept. 02-171*, revised June 2014.

Laske, G., G. Masters, Z. Ma, and M. Pasyanos (2013). Update on CRUST1.0—A 1D global model of Earth's crust, *Geophys. Res. Abstr.* **15,** Abstract EGU 2013–2658.

Li, Y.-G., J. E. Vidale, S. M. Day, D. D. Oglesby, and E. Cochran (2003). Postseismic fault healing on the rupture zone of the 1999 M 7.1 Hector Mine, California, earthquake, *Bull. Seismol. Soc. Am.* **93,** 854–869.

Massonnet, D., W. Thatcher, and H. Vadon (1996). Detection of postseismic fault-zone collapse following the Landers earthquake, *Nature* **382,** 612–616, doi: 10.1038/382612a0.

McGarr, A., B. Bekins, N. Burkardt, J. Dewey, P. Earle, W. Ellsworth, S. Ge, S. Hickman, A. Holland, E. Majer, *et al.* (2015). Coping with earthquakes induced by fluid injection, *Science* **347,** 830–831, doi: 10.1126/science.aaa0494.

McGarr, A., D. Simpson, and L. Seeber (2002). Case histories of induced and triggered seismicity, in *International Handbook of Earthquake and Engineering Seismology, Part A*, W. H. K. Lee, H. Kanamori, P. C. Jennings, and C. Kisslinger (Editors), Vol. 81A, Academic Press, Waltham, Massachusetts, 647–661.

National Research Council (2012). *Induced Seismicity Potential in Energy Technologies*, Vol. 1, The National Academies Press, Washington, D.C.

Pollitz, F. F. (1996). Coseismic deformation from earthquake faulting on a layered spherical earth, *Geophys. J. Int.* **125,** 1–14.

Rousseeuw, F. J. (1984). Least median of squares regression, *J. Am. Stat. Assoc.* **79,** 871–880, doi: 10.1080/01621459.1984.10477105.

Savage, J. C., and J. Svarc (1997). Postseismic deformation associated with the 1992 $M_w = 7.3$ Landers earthquake, southern California, *J. Geophys. Res.* **102,** 7565–7577.

Savage, J. C., M. Lisowski, and J. L. Svarc (1994). Postseismic deformation following the 1989 (M = 7.1) Loma Prieta, California, earthquake, *J. Geophys. Res.* **99,** 13,757–13,765.

Shah, A. K., and G. R. Keller (2017). Geologic influence on induced seismicity: Constraints from potential field data in Oklahoma, *Geophys. Res. Lett.* **44,** 152–161.

Sun, X., and S. Hartzell (2014). Finite-fault slip model of the 2011 M_w 5.6 Pargue, Oklahoma earthquake from regional waveforms, *Geophys. Res. Lett.* **40,** 4207–4213, doi: 10.1002/2014GL060410.

Sutherland, R., V. G. Toy, J. Townend, S. C. Cox, J. D. Eccles, D. R. Faulkner, D. J. Prior, R. J. Norris, E. Mariani, C. Boulton, *et al.* (2012). Drilling reveals fluid control on architecture and rupture of the Alpine fault, New Zealand, *Geology* **40,** 1143–1146, doi: 10.1130/G33614.1.

Waldhauser, F., and W. L. Ellsworth (2000). A double-difference earthquake location algorithm: Method and application to the northern Hayward fault, California, *Bull. Seismol. Soc. Am.* **90,** 1353–1368, doi: 10.1785/0120000006.

Walsh, F. R. I., and M. D. Zoback (2015). Oklahoma's recent earthquakes and wastewater disposal, *Sci. Adv.* **1,** no. 5, doi: 10.1126/sciadv.1500195.

Ware, R. H., D. W. Fulker, S. A. Stein, D. N. Anderson, S. K. Avery, R. D. Clark, K. K. Droegemeier, J. P. Kuettner, J. B. Minster, and S. Sorooshian (2000). SuomiNet: A real-time national GPS network for atmospheric research and education, *Bull. Am. Meteorol. Soc.* **81,** 677–694.

Wessel, P., and W. H. F. Smith (1998). New, improved version of generic mapping tools released, *Eos Trans. AGU* **79,** 579, doi: 10.1029/98EO00426.

Yeck, W. L., G. P. Hayes, D. E. MvNamara, J. L. Rubinstein, W. D. Barnhart, P. S. Earle, and H. M. Benz (2016). Oklahoma experiences largest earthquake during ongoing regional wastewater injection hazard mitigation efforts, *Geophys. Res. Lett.*, doi: 10.1002/2016GL071685.

Zoback, M. L., S. Hickman, W. Ellsworth, and the SAFOD Science Team, (2011). Scientific drilling into the San Andreas fault zone—An overview, *Sci. Drill.* **11,** 14–28, doi: 10.2204/iodp.sd.11.02.2011.

Fred F. Pollitz
Charles Wicks
U.S. Geological Survey
345 Middlefield Road, MS 977
Menlo Park, California 94025 U.S.A.
fpollitz@usgs.gov

Martin Schoenball
William Ellsworth
Department of Geophysics
Stanford University
397 Panama Mall
Stanford, California 94305 U.S.A.

Mark Murray
Department of Earth and Environmental Science
New Mexico Tech
801 Leroy Place
Socorro, New Mexico 87801 U.S.A.

Published Online 3 May 2017